

**An enhanced finite element macro-model for the  
realistic simulation of localized cracks in masonry structures:  
A large-scale application**

Savvas Saloustros<sup>a,b \*</sup>, Luca Pelà<sup>a,b</sup>, Miguel Cervera<sup>a,b</sup>, Pere Roca<sup>a,b</sup>

<sup>a</sup> *Universitat Politècnica de Catalunya (UPC-BarcelonaTech), Department of Civil and Environmental Engineering, Campus Nord, Jordi Girona 1-3, 08034, Barcelona, Spain.*

<sup>b</sup> *International Center for Numerical Methods in Engineering (CIMNE), Universitat Politècnica de Catalunya (UPC-BarcelonaTech), Gran Capitá, S/N, 08034, Barcelona, Spain*

---

\* Corresponding author.

E-mail addresses: [savvas.saloustros@upc.edu](mailto:savvas.saloustros@upc.edu) (Savvas Saloustros), [luca.pela@upc.edu](mailto:luca.pela@upc.edu) (Luca Pelà),  
[miguel.cervera@upc.edu](mailto:miguel.cervera@upc.edu) (Miguel Cervera), [pere.roca.fabregat@upc.edu](mailto:pere.roca.fabregat@upc.edu) (Pere Roca)

**Abstract** – Finite element macro-modelling approaches are widely used for the analysis of large-scale masonry structures. Despite their efficiency, they still face two important challenges: the realistic representation of damage and a reasonable independency of the numerical results to the used discretization. In this work, the classical smeared crack approach is enhanced with a crack-tracking algorithm, originating from the analysis of localized cracking in quasi-brittle materials. The proposed algorithm is for the first time applied to a large-scale wall exhibiting multiple shear and flexural cracking. Discussion covers structural aspects, as the response of the structure under different assumptions regarding the floor rigidity, but also numerical issues, commonly overlooked in the simulation of large structures, such the mesh-dependency of the numerical results.

**Keywords:** Continuum Modelling, Finite element analysis, Façades, Macro-modelling, Masonry, Mesh independency, Pushover Analysis, Shear/Flexural cracks, Strain Localization, Tracking algorithm.

**Running head:** A FE macro-model for localized cracks in large masonry structures

## 1. Introduction

The important advances of the last decades in the field of computational solid mechanics, as well as the increasing capabilities of modern computers have resulted to an ample inventory of numerical methods used for the analysis of masonry structures. Nevertheless, there is no unified approach adhering all the aspects relative to the realistic simulation of masonry, namely damage localization, geometry representation, material description, and computational efficiency. The choice of the numerical approach depends on the purpose of the structural analysis (e.g. capacity, ductility, damage origin/propagation, collapse mechanism), the complexity and scale of the structure (e.g. single structural member or whole building) and the available resources (e.g. computational cost, knowledge of geometry and material properties).

A common categorization of the various approaches is performed in terms of the detail of the material description within the numerical strategy. Under this scope, we can recognize direct numerical simulations that consider the geometry and the properties of the composite masonry material and simplified approaches that consider masonry as a homogenous material with average properties.

Direct numerical simulations of masonry originate in the pioneering work of Page (1978, 1979). Micro-modelling (Lourenco and Rots 1997, Gambarotta and Lagomarsino 1997a, Macorini and Izzudin 2011) and discrete element methods (Papastamatiou and Psycharis 1993, Lemos 1997, McInerney and DeJong 2015) are today among the most used approaches accounting for the geometry of the composite material at the scale of its constituents, i.e. mortar joints and units (brick or blocks). Corollary of this detailed modelling are realistic numerical simulations that are in very good agreement with ex-

perimental results. Nevertheless, important challenges of direct numerical simulations are the acquisition of a large number of material properties, the calibration of the numerical properties ([Sarhosis and Sheng 2014](#)) and, most importantly, the high computational cost ([Roca et al. 2010](#)). Due to these reasons, micro-modelling and discrete element approaches are up-to-date restricted to the analysis of small-scale structural elements or structures.

Numerical simulations of large masonry structures are based on a different philosophy. For large-scale computations, the direct simulation of the masonry components becomes unaffordable both in terms of model preparation and computation times. The alternative is to idealize the masonry as a homogenous material with averaged properties depending on its components. This is the assumption of a wide and diverse family of computational approaches, including equivalent frame methods ([Magenes and Calvi 1996](#), [Molins and Roca 1998](#), [Parisi and Augenti 2013](#), [Lagomarsino et al. 2013](#), [Adde- si, Liberatore and Masiani 2015](#)), numerical limit analysis ([Block and Lachauer 2013](#), [Milani 2013](#)) and continuum mechanics (or macro-modelling) finite element methods (FEM) ([Carvalho et al. 2014](#), [Pelà et al. 2014a](#), [Castellazzi et al. 2017](#)).

The macro-modelling approach has been widely used for the analysis of large masonry structures during the last decades ([Lourenço 2002](#), [Roca et al. 2010](#), [Theodossopoulos 2013](#)). Their popularity bases mostly on the facility to simulate large and complex geometries at a reasonable computational cost. FEM macro-modelling approaches can capture the structural response during the whole loading history, providing important information on the damage evolution and the subsequent collapse mechanism.

Notwithstanding the aforementioned advantages, macro-models have two important limitations. The first one concerns the representation of damage. Failure of masonry under tension, bending or shear, is characterized by localized discrete cracks. Contrary to that, the representation of damage in macro-modelling approaches is often smeared over large areas or volumes of the structure. This inconsistency with the real behaviour hampers the association of existing damage with the simulated one and may result to an inaccurate interpretation of the emerging collapse mechanism. Apart from this, the smeared crack approach in the standard irreducible formulation of the finite element method results to the erroneous damage localization that depends on the alignment of the used mesh. The problem of mesh-bias independent crack localization is an open topic within the research field of computational failure mechanics (see [Cervera, Chiumenti, and Codina 2010](#), [Rabczuk 2012](#)), with, however, limited contributions to the issues related to the analysis of large masonry structures.

To overcome the above limitations of the macro-modelling approach the authors have proposed the enhancement of the classical smeared crack approach with a local crack-tracking algorithm. This approach was introduced in ([Cervera et al. 2010](#)) with the aim of simulating localized cracks under tension or bending stress-states in quasi-brittle materials. The algorithm has been validated through comparison with experimental and analytical results on concrete and masonry structural elements ([Cervera et al. 2010](#), [Saloustros, Pelà, and Cervera 2015](#)). Aiming to account for the linear and non-linear properties of orthotropic materials, Pelà et al. ([2014](#)) coupled the algorithm with an orthotropic damage model resulting to the realistic simulation of damage experienced by timber and masonry elements. Large-scale applications include the analysis of repre-

sentative bays of the Mallorca cathedral (Roca et al. 2013, Pelà et al. 2014b) and the Poblet monastery (Petromichelakis, Saloustros, and Pelá 2014).

Despite the differences of the materials and the scale of the simulated structures, the above applications bear a common characteristic; the structural collapse is defined by cracks starting from the boundaries of the structure (e.g. wall sides, door/window openings) and propagating along one direction. Apart from these, another common failure mechanism of masonry piers and spandrels is due to diagonal shear cracking emerging from the interior and propagating along two opposite directions. Existing tracking algorithms, however, have been developed for the simulation of cracks with a single propagation direction and starting only from the boundary of the structure or predefined material perturbations. This important simplification inhibits the use of these localization approaches to the analysis of large-scale problems with diverse cracking. Aiming to extend the application field of tracking algorithms, the authors have recently proposed a novel tracking algorithm with capacity to simulate both shear and flexural cracks (Saloustros et al. 2016a, Saloustros et al. 2016b). The algorithm has been validated through comparison with an experimental result on a full-scale masonry frame.

This work investigates the applicability of the macro-model presented in (Saloustros et al. 2016a, Saloustros et al. 2016b) to the analysis of large masonry structures with failure mechanism defined by a large number of diverse cracks. To this aim, the seismic capacity of a large masonry wall is investigated by using the equivalent non-linear static analysis. To the best of the authors' knowledge, the presented analyses are the first application of tracking algorithms to the simulation of large-scale structures with multiple internal and boundary cracks. Discussion includes both the structural response of the wall under different assumptions regarding the floors' rigidity and the numerical per-

formance of classical smeared crack approach with and without the proposed crack-tracking algorithm. Special focus is given on the effect of the size and alignment of the mesh used in the numerical simulations, a topic that is rarely addressed in the existing studies about the analysis of large structures exhibiting multiple cracking.

The paper is structured as follows. [Section 2](#) outlines the underlying continuum damage model. The enhancement of the classical smeared crack approach with the tracking algorithm is presented in [Section 3](#). [Section 4](#) constitutes the core of this paper, i.e. the application of the proposed approach to the case study of a large masonry wall of an existing building. The same section covers the important issue of the mesh-dependency of the numerical simulations. The paper closes with some concluding remarks in [Section 5](#).

## **2. Continuum damage macro-model**

Damage models are appealing for large-scale computations because they do not require the costly return-mapping algorithms of plasticity models. Additionally, the use of complex failure surfaces or the combination of more than one is straightforward, as sharp changes do not affect the robustness of the computation. For these reasons, damage models have been widely used for the non-linear analysis of masonry structures ([Papa 1996](#), [Gambarotta and Lagomarsino 1997b](#), [Pelá, Cervera and Roca 2011](#)).

The material degradation is simulated in this work with the use of the continuum damage macro-model proposed by Cervera et al. ([1995](#)). The particular constitutive model considers the material as isotropic up to the triggering of the damage. In the non-linear range, there is a damaged induced orthotropy in the principal stress directions. This model has been chosen due to its good balance between computational cost and efficiency, as shown from the analysis of complex masonry structures such as the Mallor-

ca cathedral (Roca et al. 2013) and the church of the Poblet monastery (Saloustrós et al. 2014). More sophisticated models that consider the anisotropy of masonry (Trovalusci and Masiani 2003, Pelá et al. 2011, Petracca et al. 2017) can be potentially used, at the price of a higher computational cost, in cases where the anisotropic properties of the composite material are available.

In the following, the main components of the constitutive model are outlined using compact notation. Lowercase bold letters in italics stand for second order tensors (e.g.  $\boldsymbol{\sigma}$ ), uppercase bold letters in italics for fourth order tensors (e.g.  $\mathbf{C}_0$ ) and lowercase bold letters for vectors (e.g.  $\mathbf{p}_j$ ). For the detailed formulation the reader is referred to (Cervera 2003).

## 2.1 Constitutive equation

In a continuum damage model, the actual stresses of a damaged material are associated to the equivalent stresses of the intact material (i.e. the effective stresses (Chaboche 1988)) with the use of a scalar variable representing the magnitude of the damage experienced by the material. In this work, the Cauchy stress tensor  $\boldsymbol{\sigma}$  is a function of the positive and negative effective stress tensors,  $\bar{\boldsymbol{\sigma}}^+$  and  $\bar{\boldsymbol{\sigma}}^-$  respectively, through the following constitutive equation

$$\boldsymbol{\sigma} = (1 - d^+) \bar{\boldsymbol{\sigma}}^+ + (1 - d^-) \bar{\boldsymbol{\sigma}}^- \quad (1)$$

This is a model with damage induced rotating orthotropic behaviour. The scalar damage indices  $d^+$  and  $d^-$  represent the damage of the material due to tensile and compressive stress states. Their value varies from 0 for intact material to 1 for a completely damaged material. The positive and negative parts of the effective stress tensor are obtained through the following expressions (Faria, Oliver and Cervera 1998)

$$\bar{\sigma}^+ = \sum_{j=1}^3 \langle \bar{\sigma}_j \rangle \mathbf{p}_j \otimes \mathbf{p}_j \quad (2)$$

$$\bar{\sigma}^- = \bar{\sigma} - \bar{\sigma}^+ \quad (3)$$

$$\bar{\sigma} = \mathbf{C}_0 : \boldsymbol{\varepsilon} \quad (4)$$

In the above equations,  $\bar{\sigma}_j$  is the effective principal stress corresponding to the normalized eigenvector  $\mathbf{p}_j$ ,  $\mathbf{C}_0$  is the classical elastic constitutive tensor and  $\boldsymbol{\varepsilon}$  the strain tensor. Symbols  $\otimes$  and  $\langle \cdot \rangle$  stand for the tensor product and the Macaulay brackets ( $\langle x \rangle = x$ , if  $x \geq 0$ ,  $\langle x \rangle = 0$ , if  $x < 0$ ) respectively.

## 2.2 Damage criteria

The failure surfaces that determine the triggering of the  $d^+$  and  $d^-$  indices are defined through two scalar functions respectively  $\tau^\pm$  termed as the equivalent stresses

$$\tau^+ = H[\bar{\sigma}_{max}] \frac{1}{1-a} \left[ \sqrt{3\bar{J}_2} + a\bar{I}_1 + \beta \langle \bar{\sigma}_{max} \rangle \right] \frac{f^+}{f^-} \quad (5)$$

$$\tau^- = H[-\bar{\sigma}_{min}] \frac{1}{1-a} \left[ \sqrt{3\bar{J}_2} + a\bar{I}_1 + \kappa_1 \beta \langle \bar{\sigma}_{max} \rangle \right] \quad (6)$$

$$a = \frac{(f_b^-/f^-)-1}{2(f_b^-/f^-)-1} \quad (7)$$

$$\beta = (1-\alpha) \frac{f^-}{f^+} - (1+\alpha) \quad (8)$$

The above definitions show the dependence of the failure surfaces on the uniaxial tensile  $f^+$  and compressive  $f^-$  strengths, as well as on the biaxial  $f_b^-$  compressive strength.  $\bar{I}_1$  denotes the first invariant of the effective stress tensor and  $\bar{J}_2$  the second invariant of the effective deviatoric stress tensor and  $\bar{\sigma}_{max}$  and  $\bar{\sigma}_{min}$  stand for the maximum and minimum effective principal stresses respectively. The  $\kappa_1$  variable in [Equa-](#)

tion (6) has been introduced in (Petracca et al. 2015) to control the shape of the compressive failure surface in the shear quadrants. Its value ranges from 0 (leading to the Drucker-Prager criterion) to 1 (leading to the criterion proposed by Lubliner et al. (1989), see Fig. 1. Finally,  $H[\cdot]$  is the Heaviside step function ( $H[x] = 1, if x \geq 0$  and  $H[x] = 0, if x < 0$ ).

The damage criteria for tensile  $\Phi^+$  and compressive damage  $\Phi^-$  are simply

$$\Phi^\pm(r^\pm, \tau^\pm) = \tau^\pm - r^\pm \leq 0 \quad (9)$$

The scalars  $r^\pm$  represent the loading history of the material and are necessary to distinguish between loading and unloading conditions. Their initial values are equal to the tensile and compressive strength ( $r_0^+ = f^+, r_0^- = f^-$ ) of the material and then vary according to

$$r^\pm = \max[r_0^\pm, \max_{i \in (0, n)} (\tau_i^\pm)] \quad (10)$$

with  $n$  representing the number of the current (load/displacement) increment.

Finally, an exponential softening law is selected for the evolution of the damage variables

$$d^\pm = 1 - \frac{r_0^\pm}{r^\pm} \exp \left\{ 2H_d^\pm \left( \frac{r_0^\pm - r^\pm}{r_0^\pm} \right) \right\} \quad (11)$$

where  $H_d \geq 0$  is the discrete softening parameter taking into account the compressive and tensile fracture energy of the material  $G_f^\pm$  and the characteristic finite element width  $l_{dis}$ , ensuring mesh-size objective results according to the crack-band theory (Bazant and Oh 1983). Its value is defined with the following equations

$$H_d^\pm = \frac{l_{dis}}{l_{mat}^\pm - l_{dis}} \quad (12)$$

$$l_{mat}^\pm = 2EG_f^\pm / f^\pm \quad (13)$$

The value of the characteristic element width is considered as  $l_{dis} = \sqrt{2A_e}$ , where  $A_e$  is the surface of the triangular element.

### 3. The local crack-tracking algorithm

The crack-tracking algorithm serves as an enhancement of the classical smeared crack approach. Its aim is to ensure mesh-bias independency of the numerical results and the realistic representation of propagating cracks in the numerical simulation of fracture in quasi-brittle materials. The presented approach has been implemented in the finite element software COMET (2016) developed in the International Centre of Numerical Methods in Engineering (CIMNE) at the Technical University of Catalonia, Barcelona.

All the functions of the crack-tracking algorithm are performed within a set of sub-routines that are executed before the computation of the stresses at the first iteration of each (load or displacement) increment of the numerical analysis. The purpose of the algorithm is to identify the propagation path of all new and existing cracks for the current increment. A flag system is used to distinguish between (a) damaged elements, (b) non-damaged elements within a crack-path and (c) non-damaged elements outside a crack-path. The stress-strain state of the elements within the aforementioned (a) and (b) groups is defined according to the constitutive law presented in Section 2. For the elements in group (c) a linear-elastic relationship is maintained. The basic elements of the tracking algorithm are presented in Fig. 2.

The first step of the crack-tracking algorithm consists in identifying new cracks. These originate at elements satisfying the damage criterion as defined in [Equation 9](#). Since the damage condition can be satisfied for more than one element at the same increment, an “exclusion radius criterion” is used to identify the origin of a crack. This defines that the “crack root” element is the one with the highest ratio between the tensile effective stress and tensile strength of the material (i.e.  $\tau^+/f^+$ ) within an area defined by an “exclusion radius”  $r_{excl}$ . The latter value represents the minimum distance between existing and new cracks and is determined by the user. The purpose of the exclusion radius criterion is two-fold. The first one is to avoid the non-realistic spreading of damage over large areas, which typically occurs in smeared cracking problems with standard finite elements. This is a numerical pathology, not associated with the nature of the simulated material, leading in the later steps of the analysis to the erroneous and mesh-dependent localization of damage. The problem of the mesh-independent strain localization is an ongoing challenging topic in the field of computational failure mechanics, with tracking algorithms being one of the current efficient alternatives ([Cervera and Chiumenti 2006](#), [Jäger, Steinmann and Kuhl 2008](#), [Slobbe, Hendriks and Rots 2014](#), [Saloustros et al. 2015](#)). The second purpose of the exclusion radius is to account of the composite nature of the simulated material in a simplified and implicit way, when continuum finite element models are used for the numerical analysis. To illustrate this, consider the case of a historical masonry where cracking is mainly localized within the more vulnerable mortar joints, either due to the damage of the mortar or the debonding between the mortar and the (brick or stone) units. In such cases, the exclusion radius can be associated to the size of the units. A value of the exclusion radius less or equal to the finite element size recovers the classical smeared crack approach. The effect of this pa-

parameter on the simulation of masonry structures has been presented in (Cervera et al. 2010, Roca et al. 2013, Saloustros et al. 2016a, Saloustros et al. 2016b).

After recognising the new cracks for the current increment, the crack-tracking algorithm proceeds to the identification of the propagation path for each crack. The crack propagation direction is defined to be orthogonal to the direction of the maximum principal stresses as calculated either at the crack origin for new cracks or at the crack-tip element for existing ones. The crack-tip is the last element at the propagation front of a consolidated (at a previous increment) crack. For the case of internal crack origins, the crack path is sought along the two opposite orientations defined by the crack propagation vector. For crack origins lying on the boundary of the numerical domain or for crack-tips, the crack propagates to the single direction defined by the same vector.

An important task of the algorithm is the opportune correction of sudden changes in the crack propagation direction. This situation occurs for high stress gradients at the propagating front of flexural cracks. To alleviate this pathology a maximum curvature criterion is used (Cervera et al. 2010) that identifies sudden changes in the crack propagation direction at the crack-tip comparing to the last part of the crack with length  $r_{neigh}$  and corrects it according to a minimum deviation angle ( $a_{max}$ ) defined by the user. For further details, the interested reader is referred to (Cervera et al. 2010, Saloustros et al. 2016a).

#### **4. Numerical Simulation of a large-scale wall**

In this section, the enhanced macro-model with the crack-tracking algorithm is applied for the first time to the analysis of a large-scale structure with multiple cracking. The case study concerns the analysis of a five floor structural wall at the interior of a

masonry building situated in Via Martoglio, Catania Italy. The wall has regular openings symmetrically distributed along its central axis. Two irregularities exist in the structure. The first one concerns an opening at the right corner of the top floor and the second is a large door opening at the middle of the base floor. Clay brick vaults supported on concrete girders comprise the floor structural system, while the roof is a timber structure. The masonry is of regular units with dimensions  $250 \times 120 \times 55 \text{ mm}^3$  (brick UNI5628/65). All the lintels are made of masonry but that of the central door at the base, which is made of reinforced concrete. Figure 3a presents the geometry and dimensions of the analysed structure.

The numerical simulation aims to investigate the structural response of the wall against seismic actions by means of a non-linear equivalent static analysis. Two stages of loading are considered. The first one corresponds to the application of the self-weight of the walls and floors and the live load as defined in (Brencich et al. 2000). In the second stage, the seismic actions are simulated as horizontal forces applied at the level of each floor. The loading pattern is proportional to the height and the vertical loading of each floor as suggested by the Italian Code [D.M 14/01/2008].

As no information is available regarding the rigidity of the floors, two different models have been considered. In the first one (denoted hereafter as Model A), the same material parameters are used for both the masonry walls and floors assuming the existence of a flexible diaphragm (Material A in Table 1). In the second model (denoted hereafter as Model B), the floors are simulated as linear elastic with the double stiffness of the masonry aiming to consider the effect of a stiff diaphragm (Material B in Table 1). The latter material has been used in both models for modelling the lintel above the central opening at the ground floor. The material properties have been taken from previous

analyses on the same building (Brencich et al. 2000, Milani, Lourenço and Tralli 2006). The  $\kappa_1$  parameter is taken equal to 0.45 which is equivalent to assume a shear strength of 0.15 MPa, which is the value used in the previous reference studies (Brencich et al. 2000, Milani, Lourenço and Tralli 2006). The ratio between biaxial and uniaxial compression is equal to 1.15. As presented in (Saloustros et al. 2016a, Saloustros et al. 2016b), the exclusion radius can be associated to the size of units of the simulated masonry. This is because cracking usually localizes in the interface between the units and the mortar. For this reason, an exclusion radius of 0.25 m is used in this case, which is equal to the bricks length, while the rest of the tracking parameters are  $a_{max} = 45^\circ$  and  $r_{neigh} = 0.5 \text{ m}$ . The last two are minimum values that prevent the overturning of cracks. For a detailed discussion of the effect of the tracking parameters, the reader is referred to (Saloustros et al. 2016a, Saloustros et al. 2016b).

The structure is discretized using an unstructured mesh with two-dimensional constant strain triangles under plane stress conditions. The average size of the finite elements is 0.15 m resulting in a total number of 51052 elements (Fig. 3b). The analysis is performed using an arc-length method along with a line-search procedure. Convergence is achieved for a ratio between the norm of residual forces against the norm of the total external forces less than 0.01. Calculations are performed using the finite element software COMET (2016), while pre- and post-processing with GiD, developed also in CIMNE, Barcelona (GiD 2016).

#### 4.1 Model A– Flexible Diaphragm

The structural response of the Model A with flexible floors is presented in terms of base shear against top horizontal displacement in Figure 4. The structure has a maxi-

imum capacity of 635 kN. The post-peak response is characterized by a softening part leading to a residual strength of around 530 kN.

The first drop in the stiffness occurs for a base shear of around 350 kN. This coincides with the occurrence of shear and flexural cracking at the spandrels of the second and third floor as shown in [Figure 5a](#). The increase in the horizontal load results to the extension of damage to the great majority of the spandrels, see [Figure 5b](#). Flexural cracks initiate from the corner of the openings and propagate vertically within the spandrels. Contrarily, shear cracks emerge from the interior of the spandrels, at their middle height, and continue their propagation diagonally in two directions. [Figure 6](#) presents the evolution of this damage pattern for the spandrel at the 4<sup>th</sup> floor and second column of openings (counting from the right side). Cracking due to bending initiates at the two ends of the spandrel and propagates towards the interior ([Figure 6a](#)). At a later stage, shear cracks emerge at the interior ([Figure 6b](#)) of the spandrel and evolve diagonally towards the two ends of the spandrel ([Figure 6c](#)). This cracking is characteristic of a strong-pier weak spandrel configuration ([Beyer and Dazio 2012, Parisi & Augenti 2014](#)). The presented tracking algorithm can successfully simulate this common damage typology of masonry because it allows cracks to initiate at any location of the mesh and to propagate in one or two directions.

[Figure 5c](#) shows the tensile damage distribution just after the maximum capacity of the structure. The vertical piers of the right side start to behave as cantilevers owing to the extensive damage of the weak spandrels. The collapse mechanism is determined by the rotation of the right corner after the progression of damage at the spandrels of all floors of the extreme right side at levels sufficient to allow its detachment from the rest of the structure. The rest of the analysis finds the right corner rotating around its base,

resulting to important shear cracking at the base wall (Figure 5d). The analysis stops when the flexural cracks at the spandrels are entirely opened, resulting to their complete partition from their adjacent piers.

#### **4.2 Model B – Stiff Diaphragm**

The assumption of a stiff and elastic diaphragm has an important effect in the response of the structure. The capacity increases around 80%, reaching a horizontal load of 1139 kN (Figure 4). The displacement of the structure for the capacity load increases in the same order, being of 11 mm instead of 6.6 mm for Model A.

The initiation of damage is similar to that of Model A, affecting the spandrels of the second and third floor at the fourth column of openings (counting from the left side) for a base shear of around 425 kN, see Figure 7a. Contrary to Model A, the increase of the horizontal force results in a more uniform distribution of damage at the spandrels. This can be observed in Figure 7b, showing the tensile damage contour for a base shear of around 750 kN. After the spreading of damage at the spandrels, shear cracks start affecting the piers of the base floor. Important cracking seems to affect the pier next to the base door, which is probably due to a hammering effect of the rigid lintel above it. The tensile damage distribution after reaching the maximum capacity is shown in Figure 7c. The stiffer floors have restrained the rotation of the vertical piers despite the severe damage at the spandrels and mobilized the shear response of the piers. Flexural cracks start appearing at the lower left corner, while shear cracks are now evident in many piers of the structure mostly at the right side and the base. The shear failure of these piers determines the capacity of the structure, which can be seen as the drop of the base shear after the peak in the graph of Figure 4. The shear capacity of the rest piers results

to a residual strength of the structure as shown by the horizontal plateau in the post-peak response. This is followed by another sudden drop in the residual strength of the structure due to the shear failure of the rest of the piers at the left part of the structure as shown in [Figure 7d](#). The analysis stops when the shear capacity of all the base piers is exhausted.

### **4.3 Discussion of the diaphragm effect on the structural response**

The different assumptions regarding the rigidity and strength of the floors lead to substantial changes of the structural response. Stiff floors increase the integrity of the structure and the collaboration among the vertical piers even after the damage at the spandrels.

The collapse mechanism in Model A is triggered by the flexural cracking at the spandrels. This induces the cantilever behaviour of the last three vertical piers of the right side, which rotate around their base with almost no interaction among them. Failure of the structure is eventually determined by the collapse of the right side, as shown in [Figure 8a](#). Contrarily, the stiff floor in Model B results in the mobilisation of the shear response of the piers, the strength of which determines the global capacity of the structure. Collapse in this case is due to the shear failure of the piers at the base of the structure [Fig 8b](#). The capacity of the tracking algorithm to model internal cracks with two orientations, i.e. shear cracks, is crucial for the realistic simulation of the current case study.

The different nonlinear response between the shear failure and the flexural one can be appreciated through a comparison of the base shear versus displacement graphs in [Figure 4](#). Flexural failure in Model A and rocking of the vertical piers is characterized

by a smooth post-peak response. Differently, in Model B the shear failure of the piers at the base results to sudden drops in the load-carrying capacity of the structure after the peak-strength.

A common characteristic of both models is the weakness of the spandrels. The most prone of them to fail are those with massive piers at their both sides. This is the case of the spandrels at the fourth column (counting from the left side), which are the first to experience damage during the loading history (see [Figs 5a](#) and [7a](#)) for both models. Nevertheless, the damage pattern at the spandrels seems to change from mainly vertical flexural cracks to diagonal shear cracking when the floor has an increased stiffness compared to that of the masonry walls.

#### **4.4 Comparison with other approaches**

[Figure 9](#) presents a comparison between the results obtained with the macro-model proposed in this work and three alternatives from the literature: a finite element model with inserted discontinuities ([Brencich et al. 2000](#)), a limit analysis software ([Milani, Lourenço and Tralli 2006](#)) and an equivalent frame approach ([Addessi, Liberatore and Masiani 2015](#)).

The capacity obtained using Model A (635 kN) is very similar to the one calculated using the lower bound approach (691 kN) in [Milani et al. \(2006\)](#) considering the case with flexible diaphragms. The small difference may be attributed to the different application pattern of the masonry's self-weight, which was concentrated at the floor levels in ([Milani, Lourenço and Tralli 2006](#)), while here the self-weight of the walls is applied at the masonry surfaces. This difference could explain the lower capacity of the present model since more load is actually located at higher levels of the structure.

Two models are reported from the work of Brencich et al. (2000). In the Model 1 the concrete floors were assumed to have the same properties as the masonry (as in Model A here), while in Model 2 they were modelled as elastic with an elastic modulus of 5 GPa (as in Model B here). In these models, damage could localize only along discontinuities distributed within the structure at horizontal layers and separated by quadrilateral finite elements. Vertical interfaces were positioned only at the location of the masonry lintels at each floor and for a single element height. The different treatment of damage and the above restrains in the propagation of vertical cracks resulted in an increased capacity comparing to the one estimated here for both models. This difference is more important for the case of Model 1 and Model A, where the analyses show that failure is characterized by vertical cracking due to bending at the spandrels. Nevertheless, the damage distribution within the structure is equivalent in both approaches and for both models. In Models 1 and A, damage is mainly localized at the spandrels, while in Models 2 and B significant damage affects the piers of the structure, and especially those of the lower floor.

Finally, the maximum capacity obtained using Model B is very close to the one predicted in (Addessi, Liberatore and Masiani 2015) for a model with the assumption of elastic diaphragms and using an equivalent frame approach with force-based beam finite elements. The differences existing in the linear response are due to the use of a different value of elastic modulus for the walls of the structure.

The obtained results using the proposed approach are in overall agreement with those existing in the literature. The enhanced capacity of the crack-tracking algorithm to simulate the propagation of damage within the structure results to a more detailed representation of the post-peak response, as shown especially for the case of Model B. The

presented approach can be an efficient alternative for the analysis of large structures, especially when the analyst necessitates information regarding the behaviour of the different structural members and the local collapse mechanisms occurring within the structure.

#### **4.5 Mesh dependency**

This section investigates the dependency of the proposed approach to the discretization size and structure of the mesh. The performed analyses consider the properties of Model A using two additional meshes, and the obtained results are compared with the reference mesh of [Figure 3b](#).

##### **4.5.1 Mesh-size dependency**

The mesh-size dependency is investigated using a refined unstructured mesh with average element size equal to 75 mm. This increased refinement results in a total number of 204729 elements, i.e. 4 times more than in the reference model. The difference of the refinement level is illustrated in [Figure 10](#).

[Figure 11](#) shows the global response of the structure for the two unstructured meshes with the different element sizes. The two graphs almost coincide providing identical capacity for both cases and a very similar post-peak response. As illustrated in [Figure 12a](#), the damage pattern is comparable for both cases. The same occurs for the obtained collapse mechanism, shown with the contour of the maximum principal strains in [Figure 12b](#). The proposed enhanced macro-model gives results that are mesh-size independent. This is due to both the correct localization of the damage and the regularization of the constitutive law according to the finite element's characteristic length as shown from Equations (11)-(13).

#### 4.5.2 Mesh-bias dependency

The mesh-bias dependency is investigated by comparing the results obtained with the mesh of [Figure 3b](#), with a structured mesh presented in [Figure 13](#). The sides of the orthogonal triangles make angles of  $0^\circ$ ,  $45^\circ$ ,  $90^\circ$  and  $135^\circ$  with the horizontal direction and have a mean length of 150 mm (44852 elements). Analyses with this mesh are carried-out with both the classical smeared crack approach and the crack-tracking algorithm.

The damage distribution as well as the localized strains for a horizontal displacement of approximately 21 mm using the two different meshes and the enhanced macro-model are presented in [Figure 14](#). The obtained results are in good agreement. The damage typology at the spandrels is similar in both cases, with flexural cracks being present at the two corners of the openings and shear cracks at the middle of the spandrels. Good agreement is found also for the localized cracks and the occurring collapse mechanism, determined by the overturning of the right corner as shown in [Figure 14b](#) and [Figure 14d](#).

The effectiveness of the crack-tracking technique to address the mesh-bias dependency is better demonstrated when compared with the numerical simulations carried-out without using the algorithm. To this aim, both meshes of [Figure 3b](#) and [Figure 13](#) are analysed using the classical smeared crack approach. [Figure 15a](#) presents the contours of tensile damage using the unstructured mesh of [Figure 3b](#), for a horizontal displacement at the top of the structure equal to 15.4 mm. Severe damage affects the spandrel walls resulting to their separation from the adjacent piers and the rotation of the vertical walls at the right side of the structure. Note the direction of the cracks that have opened during the loading history, but also the open cracks after reaching the capacity of the structure ([Figure 15b](#)); they are mostly diagonal, referring to a prevailing shear failure at

the spandrels. Consider now the results of the numerical analysis using the structured mesh of [Figure 13](#). [Figure 15c](#) presents the contour of the tensile damage for a displacement of 15.5 mm at the top of the structure. Cracking once again prevails at the spandrels, but this time the crack orientation is vertical in the great majority of the existing cracks. This is better observed with the contour of the maximum principal strains showing the localized cracks in [Figure 15d](#).

It is obvious that the numerical solution is mesh-bias dependent for both the used discretizations when the proposed enhanced macro-model is not used. This numerical pathology inhibits the assessment of the actual local collapse mechanisms. On the contrary, the proposed algorithm shows to be robust, even for the structured mesh with orientations that facilitate the opening of vertical cracks, as the case of the classical smeared crack approach has demonstrated.

The different response of the structure for the two meshes is clear in the base shear against horizontal displacement graphs of [Figure 16](#). The capacity of the structure without the use of the crack-tracking algorithm is lower by around 14% when the structured mesh is used, compared to the result with the structured one. This is due to the mesh-biased cracking at the spandrels, being vertical at the case of the structured mesh and diagonal for the unstructured one. Quite different response is also observed in the post-peak range with a sharper decrease of the residual capacity. Contrarily, the results using the crack-tracking algorithm are in good agreement among them for both used meshes ([Figure 16](#)). The capacity is lower by around 2% for the case with the structured mesh. Despite this, the structural response is clearly similar for both cases, even in the post-peak response. A comparison between the graphs obtained with and without the track-

ing algorithm reveals the impact of the erroneous localization of damage with the smeared crack approach.

## **5. Conclusions**

In this work, an enhanced continuum finite element model has been applied to the analysis of a large masonry structure. The model bases in the use of standard finite elements, a crack-tracking algorithm and a continuum damage model.

The proposed enhanced continuum finite element model has been used for the non-linear analysis of a real case study consisting of a large masonry façade of an existing building, for the combined gravitational loads and (earthquake equivalent) monotonically increasing horizontal forces. The use of the proposed algorithm has given an important insight on the alteration of the structural response of the simulated wall for the two different assumptions regarding the rigidity of the floor system. A flexible diaphragm results to a reduced capacity and to a collapse mechanism characterized by the cantilever response of the vertical continuous piers after flexural and shear damage in the weak spandrels. The horizontal loading finally evokes the complete separation of the right side of the structure. On contrary, a floor system with increased stiffness and strength (compared to the vertical walls) preserves the integrity of the structure after the shear damage of the spandrels. Failure in this case is characterized by shear cracking at the piers of the base floor.

Numerical analyses carried out using various discretizations with different sizes and orientations demonstrate the mesh-size and mesh-bias independency of the proposed approach. For the mesh-bias dependency study, the enhanced model with the tracking method has been compared with the traditional smeared crack approach. The obtained

crack pattern using the classical smeared crack approach has shown to depend notably on the orientation of the mesh, affecting considerably the structural response and the predicted capacity of the analysed wall. On the contrary, the results obtained with the crack-tracking algorithm have been very consistent for both meshes. The proposed approach has shown to be robust and suitable for the realistic simulation of multiple cracking in large structures.

## **Acknowledgments**

This research has received the financial support from the MINECO (Ministerio de Economía y Competitividad of the Spanish Government) and the ERDF (European Regional Development Fund) through the the MULTIMAS project (Multiscale techniques for the experimental and numerical analysis of the reliability of masonry structures, ref. num. BIA2015-63882-P) and the EACY project (Enhanced accuracy computational and experimental framework for strain localization and failure mechanisms, ref. num MAT 2013-48624-C2-1-P).

## 6. Figure Captions

Figure 1. The damage surface as proposed in (Lubliner et al. 1989)

Figure 2. The basic elements of the crack-tracking algorithm

Figure 3. (a) Geometry of the analysed wall (in mm) and (b) the used unstructured mesh.

Figure 4. Base shear versus horizontal displacement at the top right corner of the structure for the flexible diaphragm case (Model A) and for the stiff diaphragm case (Model B).

Figure 5. Tensile damage contour of Model A for a horizontal displacement at the right top of: (a) 2 mm (point A1 in Figure 4), (b) 3.5 mm (point B1 in Figure 4), (c) 6.9 mm (point C1 in Figure 4) and (d) 37 mm (point D1 in Figure 4).

Figure 6. Flexural and shear cracking evolution at the spandrel of the 4<sup>th</sup> floor, second column of openings (counting from the right side) for a displacement at the top of: (a)  $u = 2.9$  mm (b)  $u = 4.0$  mm (c)  $u = 11.9$  mm.

Figure 7. Tensile damage contour of Model B for a horizontal displacement at the right top of: (a) 2.2 mm (point A2 in Figure 4), (b) 4.8 mm (point B2 in Figure 4), (c) 11.4 mm (point C2 in Figure 4) and (d) 25.1 mm (point D2 in Figure 4).

Figure 8. Contour of the maximum principal strains on a deformed ( $\times 30$ ) mesh for (a) Model A and (b) Model B.

Figure 9. Comparison of the global response of the Via Martoglio masonry wall as obtained by different numerical approaches.

Figure 10. Part of the mesh used with average element size of (a)  $h_e = 150$  mm, (b)  $h_e = 75$  mm.

**Figure 11.** Base shear versus horizontal displacement at the top right corner of the structure using a mesh with different element size.

**Figure 12.** Contours of (a) tensile damage, (b) maximum principal strains on a deformed ( $\times 40$ ) mesh for a displacement at the top right corner of 37 mm. Top row: unstructured mesh with average element size of 150 mm, Bottom row: unstructured mesh with average element size of 75 mm.

**Figure 13.** Structured mesh used in the mesh-bias sensitivity analysis.

**Figure 14.** Simulation of Model A using the proposed crack-tracking algorithm. (a) Tensile damage and (b) maximum principal strains using the unstructured mesh for a horizontal displacement of 20.9 mm (Point 1 in **Figure 11**). (c) Tensile damage and (d) maximum principal strains using the structured mesh for a horizontal displacement of 21.2 mm (Point 2 in **Figure 11**).

**Figure 15.** Simulation of Model A using the classical smeared crack approach. (a) Tensile damage and (b) maximum principal strains using the unstructured mesh for a horizontal displacement of 15.4 mm (Point 3 in **Figure 11**). (c) Tensile damage and (d) maximum principal strains using the structured mesh for a horizontal displacement of 15.5 mm (Point 4 in **Figure 11**).

**Figure 16.** Base shear versus horizontal displacement at the top right corner of the structure using two different meshes (structured and unstructured), with and without the proposed crack-tracking algorithm.

## 7. Tables

Material	$\gamma$ ( $kg/m^3$ )	$E$ ( $MPa$ )	$\nu$ (-)	$f^+$ ( $MPa$ )	$f^-$ ( $MPa$ )	$G_f^+$ ( $J/m^2$ )	$G_f^-$ ( $J/m^2$ )	Model A	Model B
A	1700	2500	0.2	3.00	0.1	100	50000	Wall & Floors	Walls
B	1700	5000	0.2	-	-	-	-	Lintel	Lintel & Floors

Table 1 Material parameters adopted in the numerical simulations

## 8. Figures

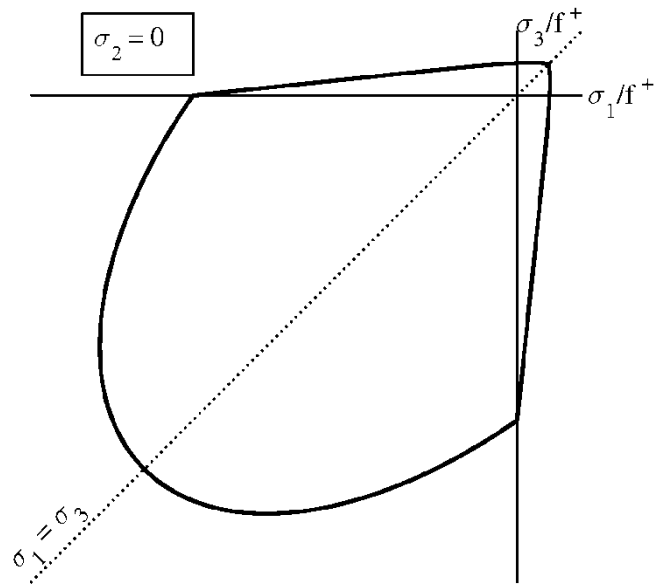


Figure 1. The damage surface as proposed in (Lubliner et al. 1989)

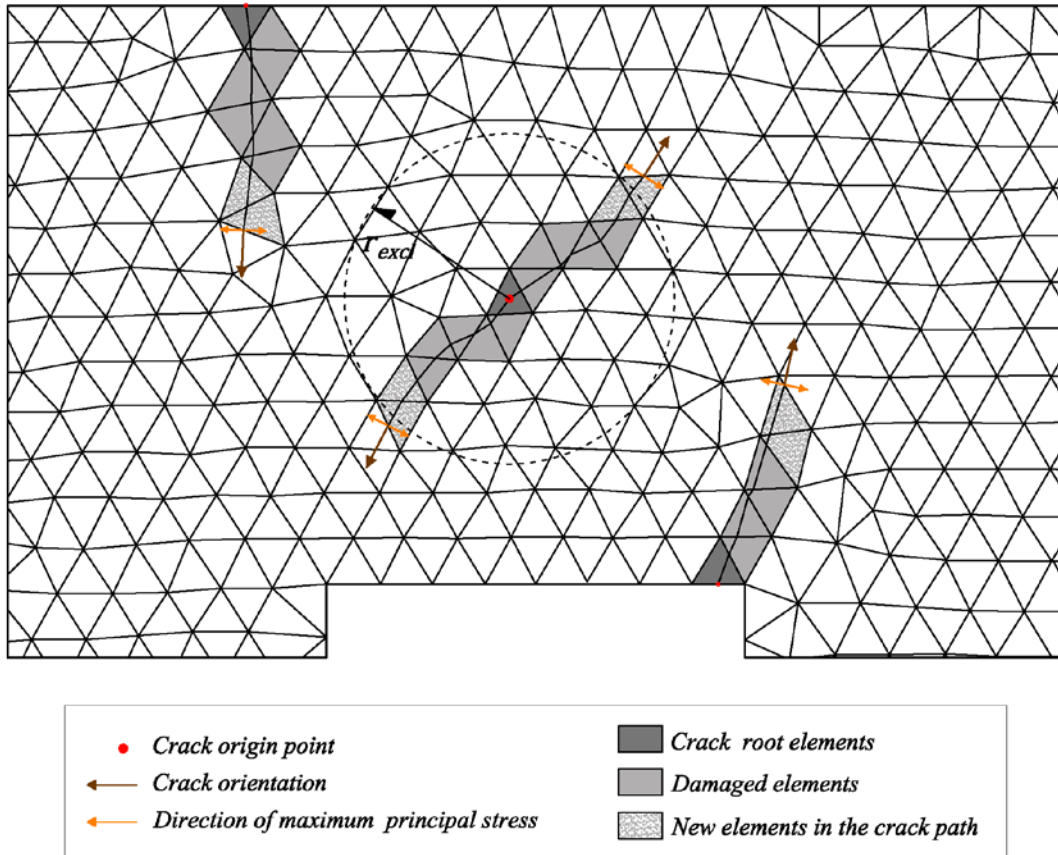
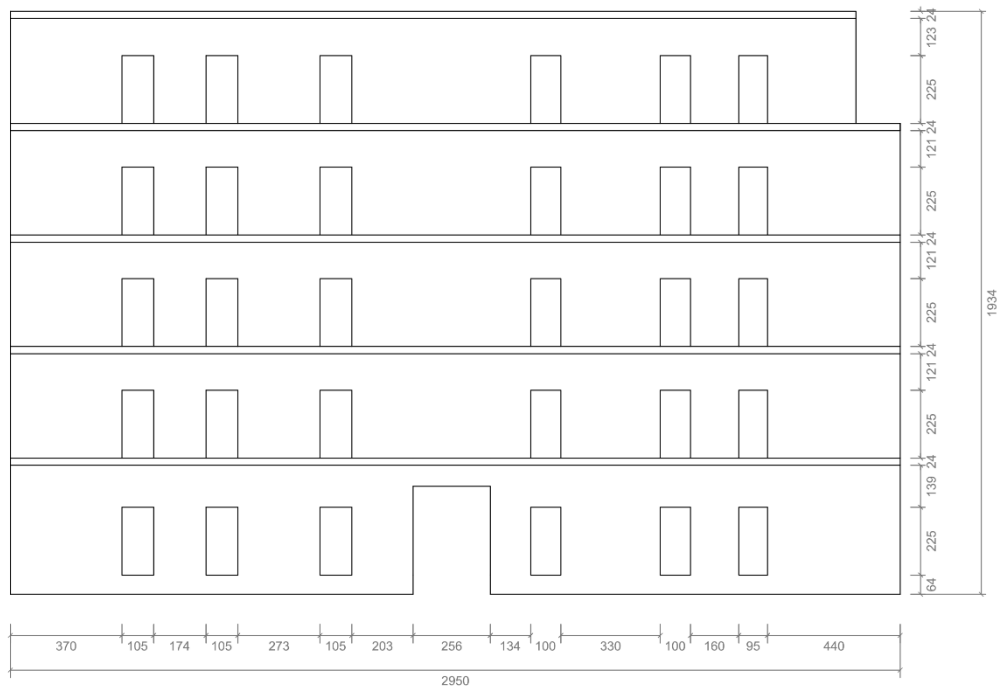
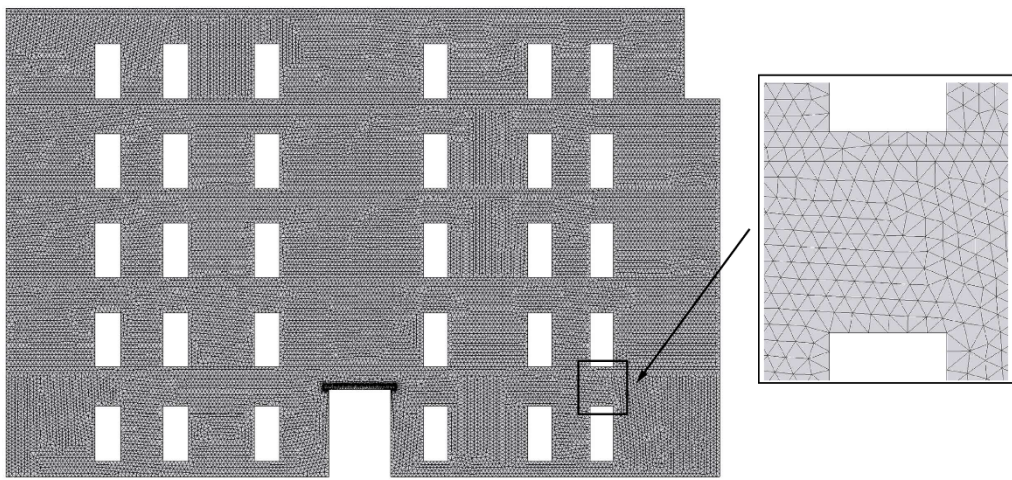


Figure 2. The basic elements of the crack-tracking algorithm



(a)



(b)

Figure 3. (a) Geometry of the analysed wall (in mm) and (b) the used unstructured mesh.

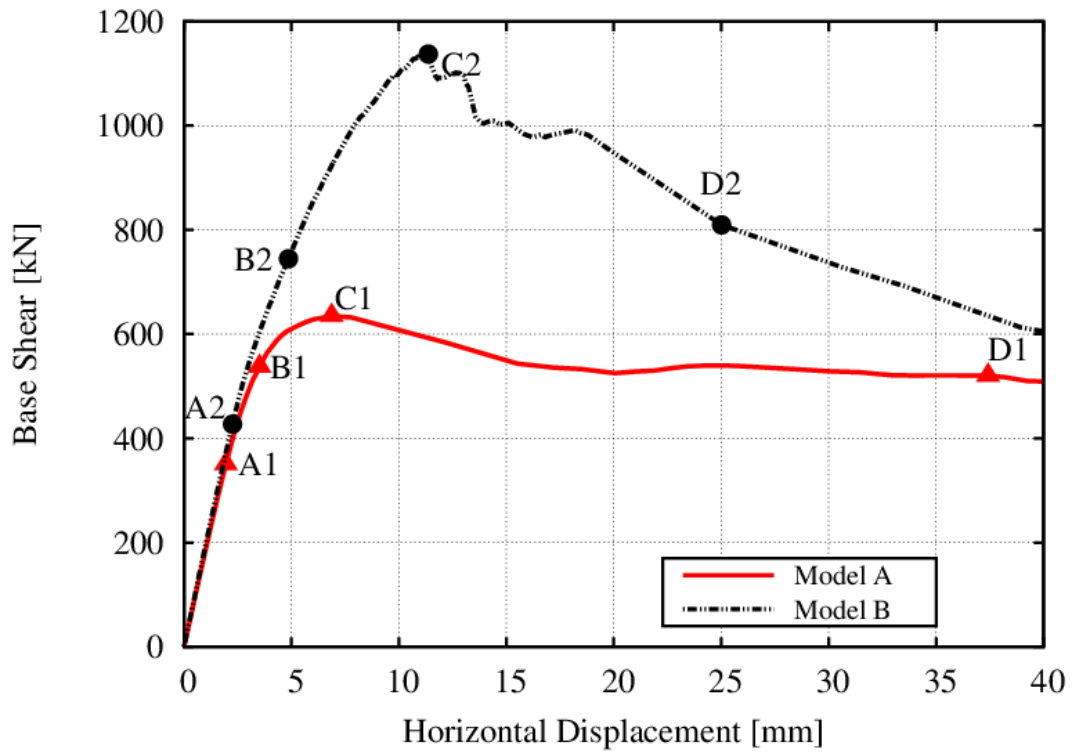
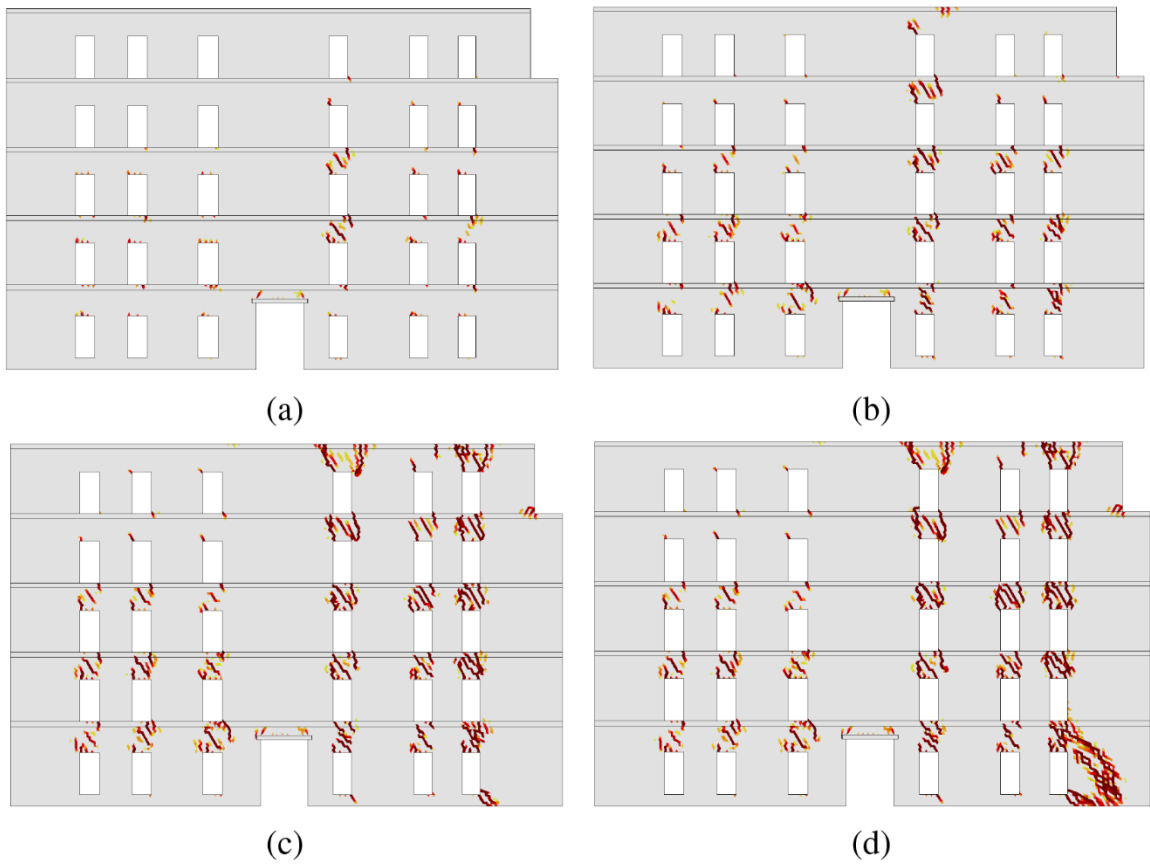
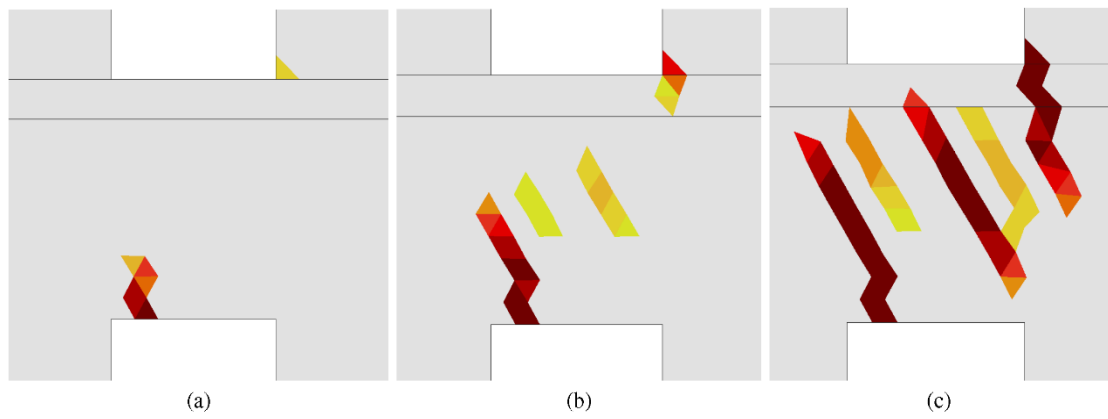


Figure 4. Base shear versus horizontal displacement at the top right corner of the structure for the flexible diaphragm case (Model A) and for the stiff diaphragm case (Model B).



**Figure 5.** Tensile damage contour of Model A for a horizontal displacement at the right top of: (a) 2 mm (point A1 in [Figure 4](#)), (b) 3.5 mm (point B1 in [Figure 4](#)), (c) 6.9 mm (point C1 in [Figure 4](#)) and (d) 37 mm (point D1 in [Figure 4](#)).



**Figure 6.** Flexural and shear cracking evolution at the spandrel of the 4<sup>th</sup> floor, second column of openings (counting from the right side) for a displacement at the top of: (a)  $u = 2.9$  mm (b)  $u = 4.0$  mm (c)  $u = 11.9$  mm.

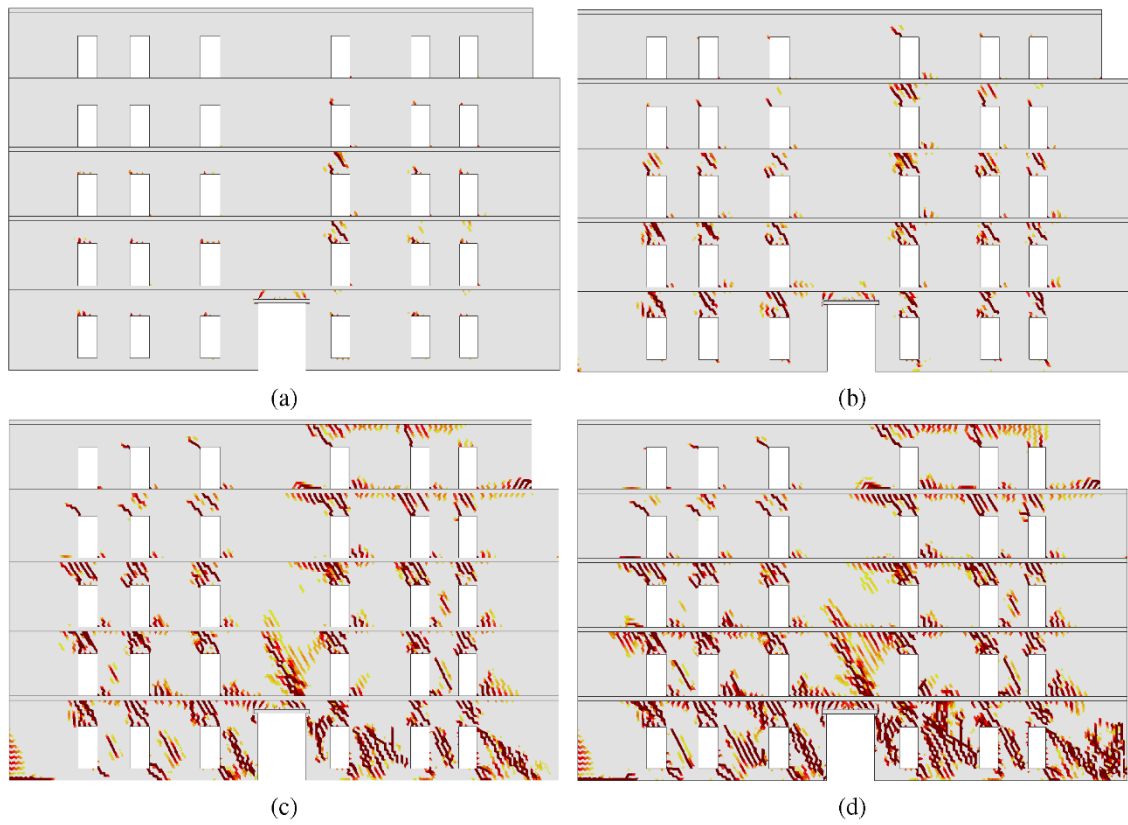
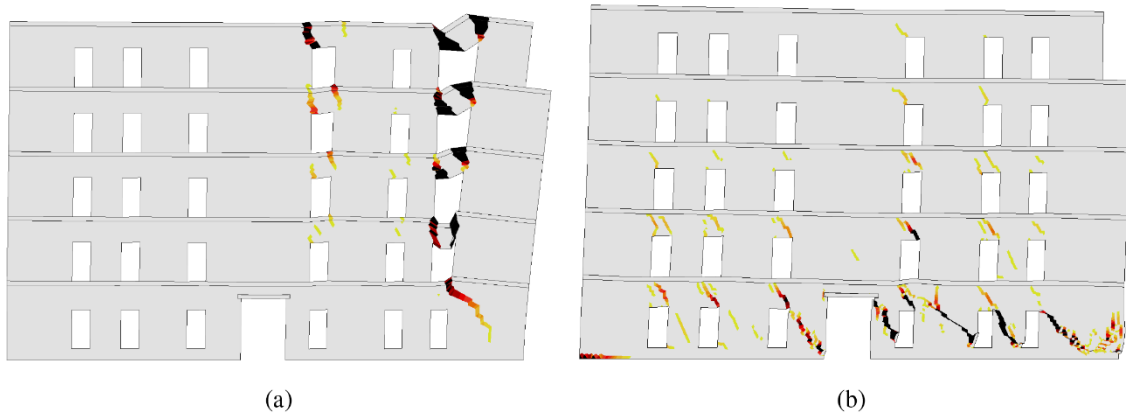


Figure 7. Tensile damage contour of Model B for a horizontal displacement at the right top of: (a) 2.2 mm (point A2 in Figure 4), (b) 4.8 mm (point B2 in Figure 4), (c) 11.4 mm (point C2 in Figure 4) and (d) 25.1 mm (point D2 in Figure 4).



**Figure 8.** Contour of the maximum principal strains on a deformed ( $\times 30$ ) mesh for (a) Model A and (b) Model B.

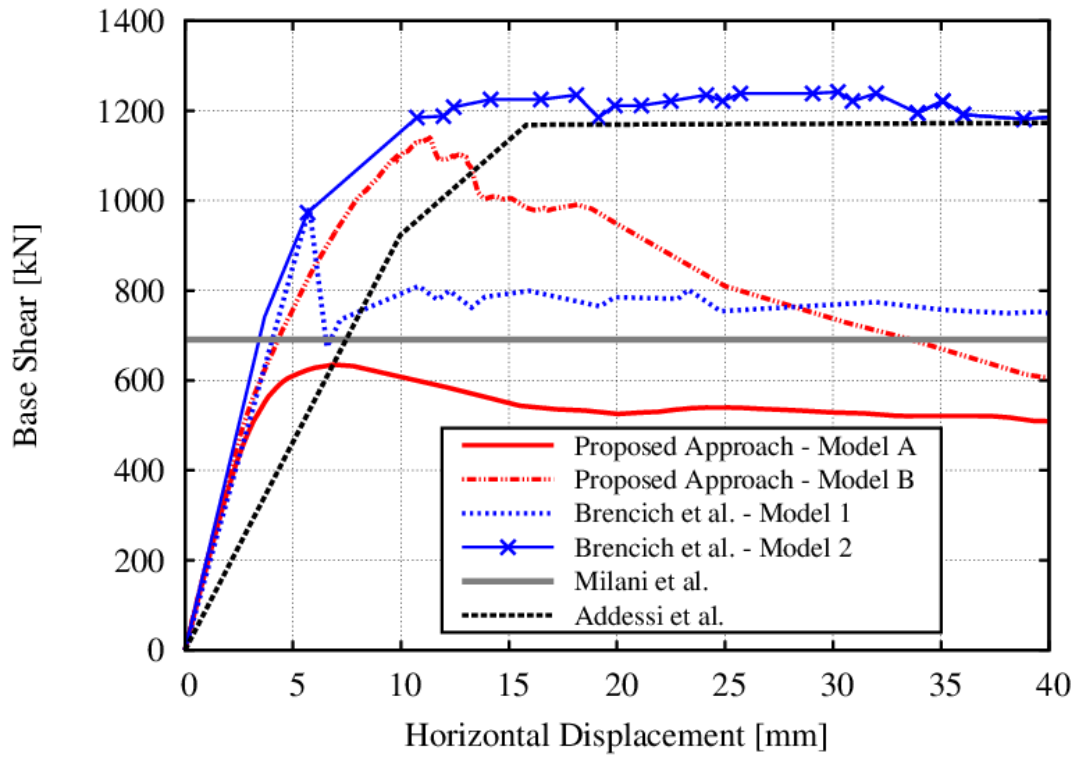


Figure 9. Comparison of the global response of the Via Martoglio masonry wall as obtained by different numerical approaches.

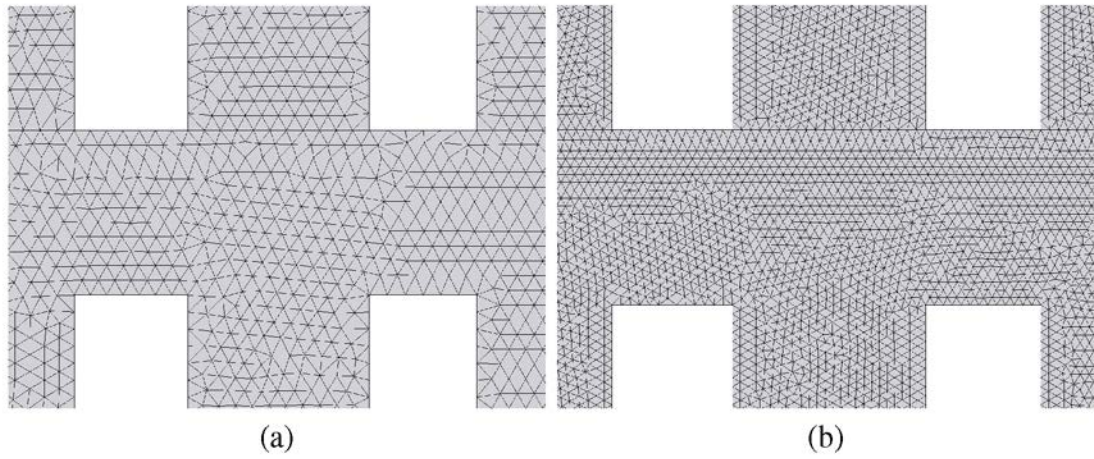


Figure 10. Part of the mesh used with average element size of (a)  $h_e = 150 \text{ mm}$ , (b)  $h_e = 75 \text{ mm}$ .

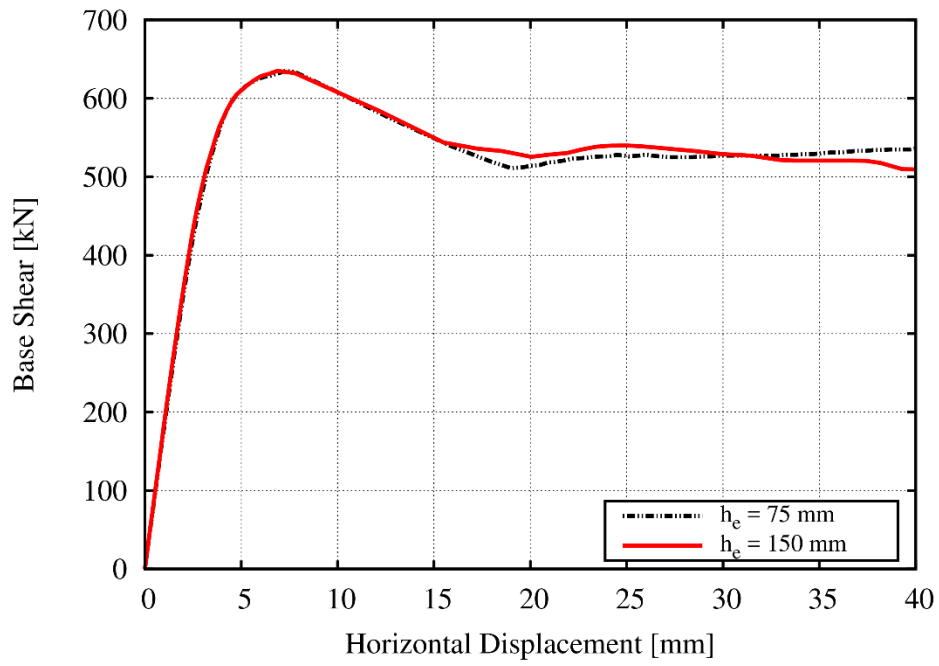


Figure 11. Base shear versus horizontal displacement at the top right corner of the structure using a mesh with different element size.

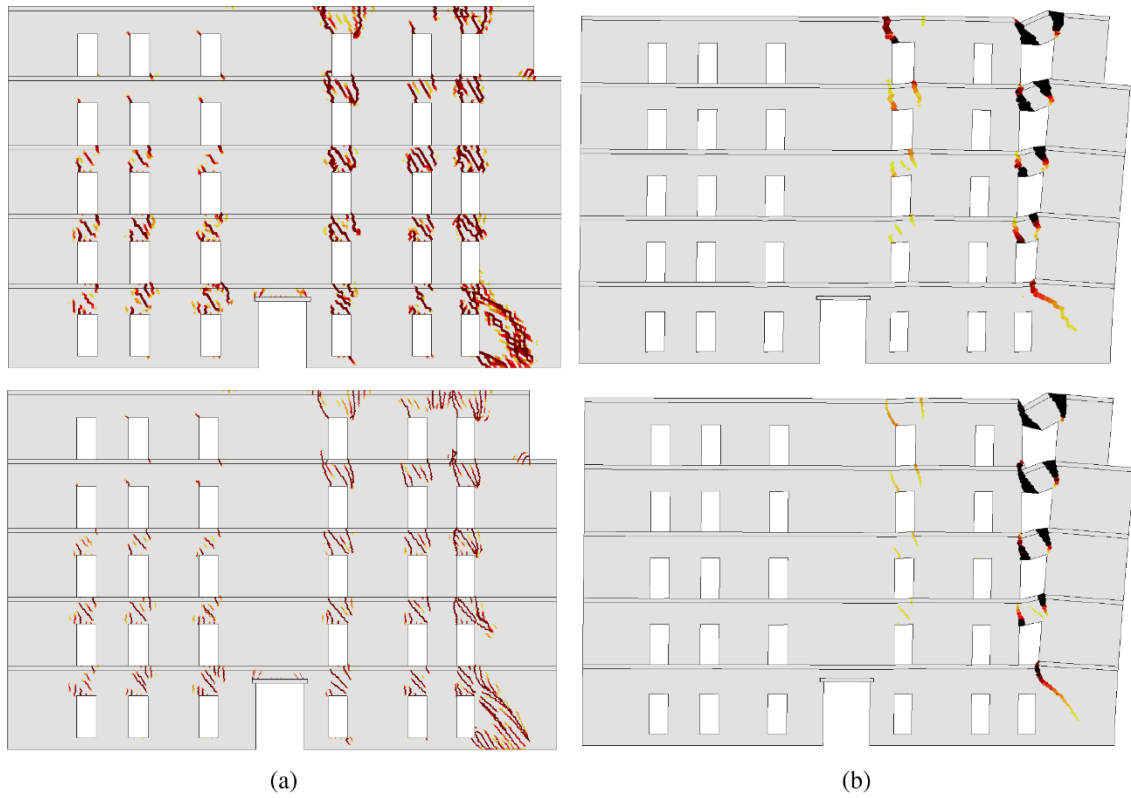


Figure 12. Contours of (a) tensile damage, (b) maximum principal strains on a deformed ( $\times 40$ ) mesh for a displacement at the top right corner of 37 mm. Top row: unstructured mesh with average element size of 150 mm, Bottom row: unstructured mesh with average element size of 75 mm.

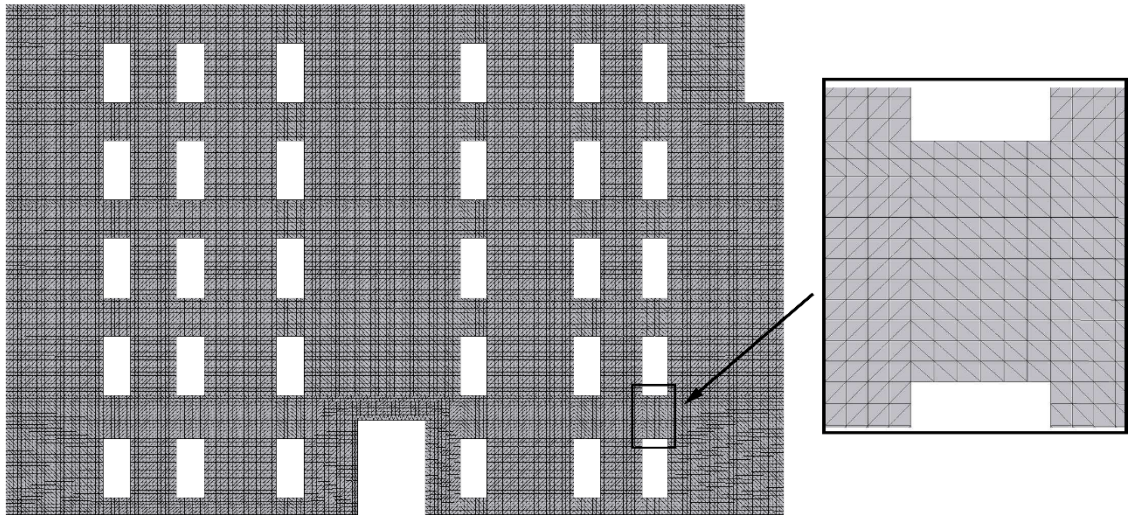
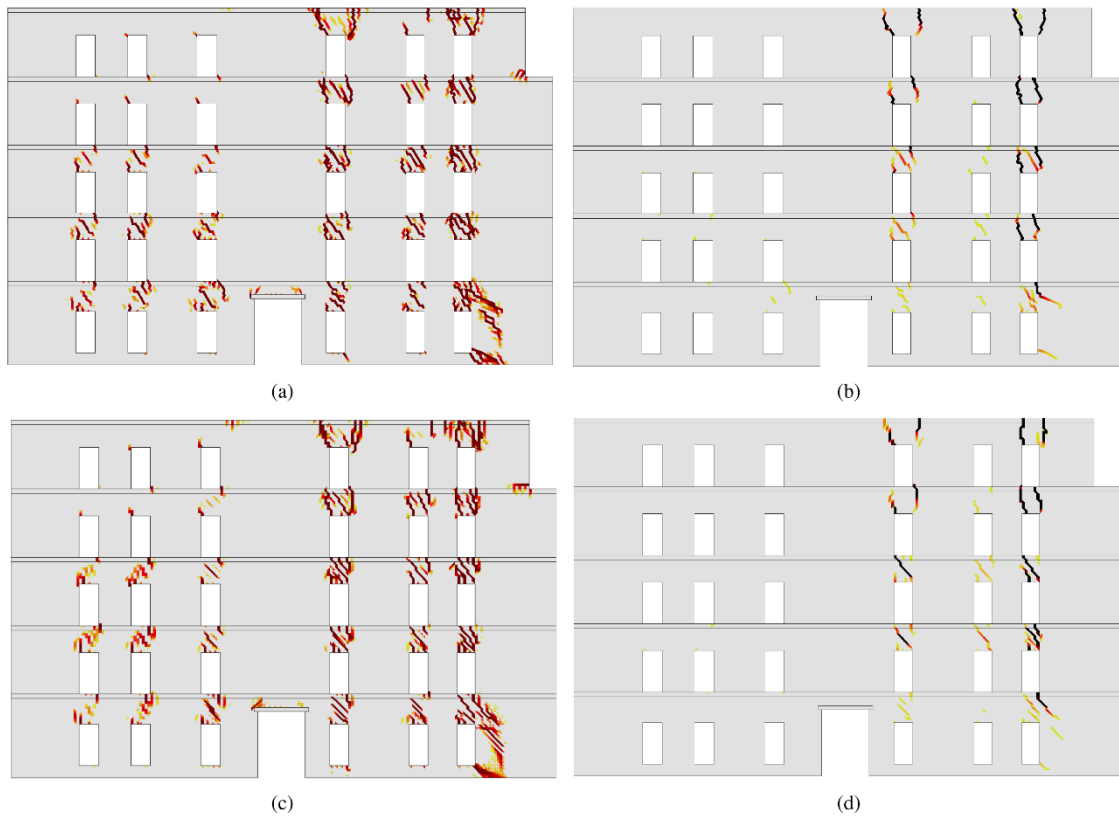
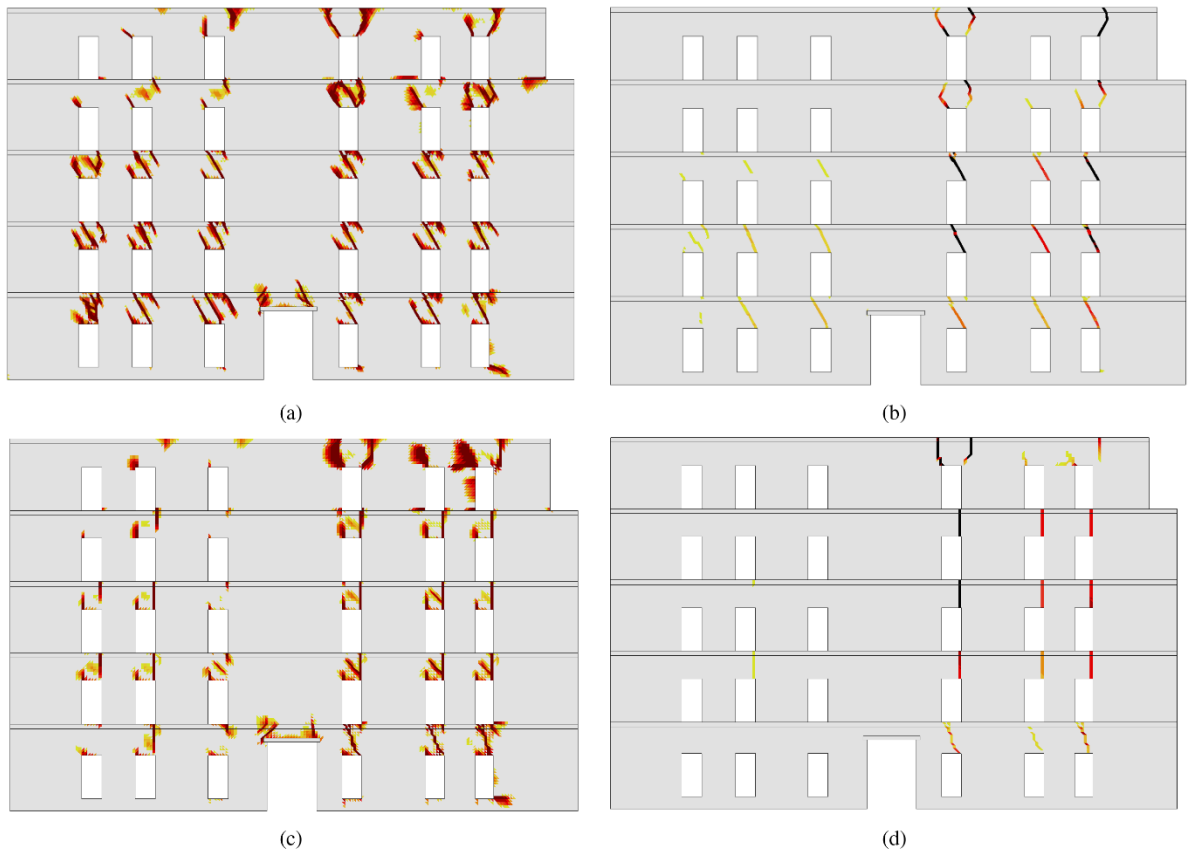


Figure 13. Structured mesh used in the mesh-bias sensitivity analysis.



**Figure 14.** Simulation of Model A using the proposed crack-tracking algorithm. (a) Tensile damage and (b) maximum principal strains using the unstructured mesh for a horizontal displacement of 20.9 mm (Point 1 in [Figure 11](#)). (c) Tensile damage and (d) maximum principal strains using the structured mesh for a horizontal displacement of 21.2 mm (Point 2 in [Figure 11](#)).



**Figure 15.** Simulation of Model A using the classical smeared crack approach. (a) Tensile damage and (b) maximum principal strains using the unstructured mesh for a horizontal displacement of 15.4 mm (Point 3 in [Figure 11](#)). (c) Tensile damage and (d) maximum principal strains using the structured mesh for a horizontal displacement of 15.5 mm (Point 4 in [Figure 11](#)).

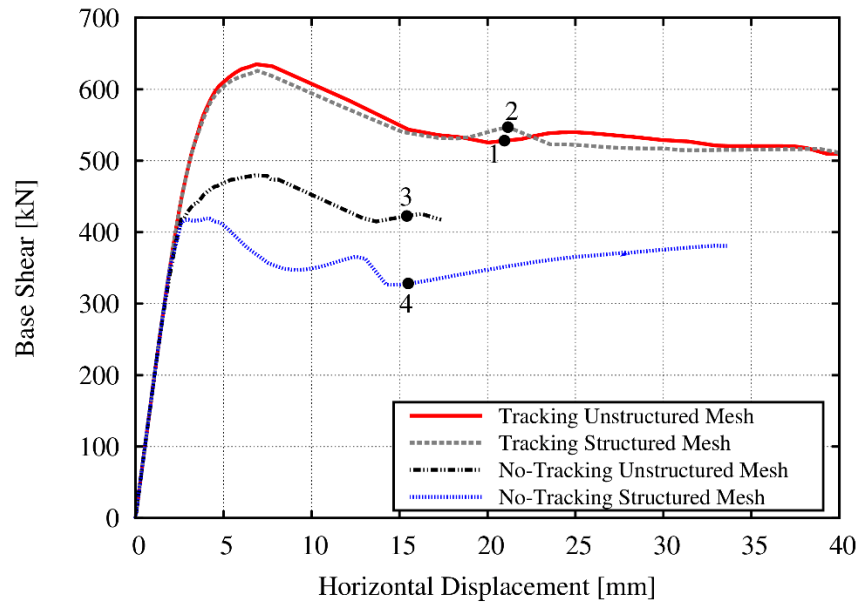


Figure 16. Base shear versus horizontal displacement at the top right corner of the structure using two different meshes (structured and unstructured), with and without the proposed crack-tracking algorithm.



## 9. References

Addressi, D, D Liberatore, and R Masiani. 2015. “Force-Based Beam Finite Element (FE) for the Pushover Analysis of Masonry Buildings.” *International Journal of Architectural Heritage* 9 (3). Taylor & Francis: 231–43. doi:10.1080/15583058.2013.768309.

Bazant, Z., and B. Oh. 1983. “Crack Band Theory for Fracture of Concrete.” *Materials and Structures* 16: 155–77. doi:10.1007/BF02486267.

Beyer, K., and A. Dazio. 2012. “Quasi-Static Cyclic Tests on Masonry Spandrels.” *Earthquake Spectra* 28 (3). Earthquake Engineering Research Institute: 907–29. doi:10.1193/1.4000063.

Block, P., and L. Lachauer. 2013. “Three-Dimensional (3D) Equilibrium Analysis of Gothic Masonry Vaults.” *International Journal of Architectural Heritage* 8 (3): 312–35. doi:10.1080/15583058.2013.826301.

Brencich, A, L Gambarotta, and S Lagomarsino. 2000. “Catania Project: Research on the Seismic Response of Two Masonry Buildings. Chapter 6: Analysis of a Masonry Building in Via Martoglio.” *CNR Gruppo Nazionale per La Difesa Dei Terremoti*, 107–43.

Carvalho, J., J. Ortega, P. B. Lourenço, L. F. Ramos, and H. Roman. 2014. “Safety Analysis of Modern Heritage Masonry Buildings: Box-Buildings in Recife, Brazil.” *Engineering Structures* 80. Elsevier Ltd: 222–40. doi:10.1016/j.engstruct.2014.09.004.

Castellazzi, G., A. M. D’Altri, S. de Miranda, and F. Ubertini. 2017. “An Innovative Numerical Modeling Strategy for the Structural Analysis of Historical Monumental

Buildings.” *Engineering Structures* 132. Elsevier Ltd: 229–48.  
doi:10.1016/j.engstruct.2016.11.032.

Cervera, M., J. Oliver, and R. Faria. 1995. “Seismic Evaluation of Concrete Dams via Continuum Damage Models.” *Earthquake Engineering & Structural Dynamics* 24 (9): 1225–45. <http://onlinelibrary.wiley.com/doi/10.1002/eqe.4290240905/abstract>.

Cervera, M., and M. Chiumenti. 2006. “Smearred Crack Approach: Back to the Original Track.” *International Journal for Numerical and Analytical Methods in Geomechanics* 30 (12): 1173–99. doi:10.1002/nag.518.

Cervera, M., L. Pelà, R. Clemente, and P. Roca. 2010. “A Crack-Tracking Technique for Localized Damage in Quasi-Brittle Materials.” *Engineering Fracture Mechanics* 77 (13). Elsevier Ltd: 2431–50. doi:10.1016/j.engfracmech.2010.06.013.

Cervera, M., M. Chiumenti, and R. Codina. 2010. “Mixed Stabilized Finite Element Methods in Nonlinear Solid Mechanics. Part II: Strain Localization.” *Computer Methods in Applied Mechanics and Engineering* 199 (37–40). Elsevier B.V.: 2571–89. doi:10.1016/j.cma.2010.04.005.

Chaboche, J. L. 1988. “Continuum Damage Mechanics: Part I—General Concepts.” *Journal of Applied Mechanics* 55 (1). American Society of Mechanical Engineers: 59. doi:10.1115/1.3173661.

COMET. 2016. “Coupled Mechanical and Thermal Analysis, [Http://www.cimne.com/comet/](http://www.cimne.com/comet/).” Barcelona. <http://www.cimne.com/comet/>.

D.M.14/01/2008. 2008. “Approvazione Delle Nuove Norme Tecniche per Le Costruzioni.” Rome, Italy.

Faria, R., J. Oliver, and M. Cervera. 1998. "A Strain-Based Plastic Viscous-Damage Model for Massive Concrete Structures." *International Journal of Solids and Structures* 35 (14): 1533–58. doi:10.1016/S0020-7683(97)00119-4.

Gambarotta, L., and S. Lagomarsino. 1997a. "Damage Models for the Seismic Response of Brick Masonry Shear Walls. Part I: The Mortar Joint Model and Its Applications." *Earthquake Engineering and Structural Dynamics* 26 (4): 423–39. <http://www.scopus.com/inward/record.url?eid=2-s2.0-0031126521&partnerID=tZOtx3y1>.

Gambarotta, L., and S. Lagomarsino. 1997b. "Damage Models for the Seismic Response of Brick Masonry Shear Walls. Part I: The Mortar Joint Models and Its Applications." *Earthquake Engineering and Structural Dynamics* 26 (March 1996): 423–39. doi:10.1002/(SICI)1096-9845(199704)26:4<441::AID-EQE651>3.0.CO;2-0.

GiD. 2016. "The Personal Pre and Post-Processor, <Http://www.gidhome.com/>." Barcelona. <http://www.gidhome.com/>.

Jäger, P., P. Steinmann, and E. Kuhl. 2008. "Modeling Three-Dimensional Crack Propagation-A Comparison of Crack Path Tracking Strategies." *International Journal for Numerical Methods in Engineering* 76 (9): 1328–52. doi:10.1002/nme.2353.

Lagomarsino, S., A. Penna, A. Galasco, and S. Cattari. 2013. "TREMURI Program: An Equivalent Frame Model for the Nonlinear Seismic Analysis of Masonry Buildings." *Engineering Structures* 56. Elsevier Ltd: 1787–99. doi:10.1016/j.engstruct.2013.08.002.

Lemos, J.V. 2007. "Discrete Element Modeling of Masonry Structures." *International Journal of Architectural Heritage* 1 (2): 190–213. doi:10.1080/15583050601176868.

Lourenço, P. B., and J. G. Rots. 1997. “Multisurface Interface Model for Analysis of Masonry Structures.” *Journal of Engineering Mechanics* 123 (7): 660–68. doi:10.1061/(ASCE)0733-9399(1997)123:7(660).

Lourenço, P. B. 2002. “Computations on Historic Masonry Structures.” *Progress in Structural Engineering and Materials* 4 (3): 301–19. doi:10.1002/pse.120.

Lubliner, J., J. Oliver, S. Oller, and E. Oñate. 1989. “A Plastic-Damage Model for Concrete.” *International Journal of Solids and Structures* 25 (3): 299–326. doi:10.1016/0020-7683(89)90050-4.

Macorini, L., and B. A. Izzuddin. 2011. “A Non-Linear Interface Element for 3D Mesoscale Analysis of Brick-Masonry Structures.” *International Journal for Numerical Methods in Engineering* 85 (12): 1584–1608. doi:10.1002/nme.3046.

Magenes, G., and G.M. Calvi. 1996. “Prospettive per La Calibrazione Di Metodi Semplificati per L’analisi Sismica Di Pareti Murarie.” In *Atti Del Convegno Nazionale “La Meccanica Delle Murature Tra Teoria E Progetto,”* edited by Pitagora Ed. Messina, Italy.

McInerney, J., and M. DeJong. 2015. “Discrete Element Modeling of Groin Vault Displacement Capacity.” *International Journal of Architectural Heritage* 9 (8): 1037–49. doi:10.1080/15583058.2014.923953.

Milani, G., P.B. Lourenço, and A. Tralli. 2006. “Homogenised Limit Analysis of Masonry Walls, Part II: Structural Examples.” *Computers & Structures* 84 (3–4): 181–95. doi:10.1016/j.compstruc.2005.09.004.

Milani, G.. 2013. “Lesson Learned after the Emilia-Romagna, Italy, 20–29 May 2012 Earthquakes: A Limit Analysis Insight on Three Masonry Churches.” *Engineering Fail-*

ure Analysis 34 (December). Elsevier Ltd: 761–78.  
doi:10.1016/j.engfailanal.2013.01.001.

Molins, C., and P. Roca. 1998. “Capacity of Masonry Arches and Spatial Frames.” *Journal of Structural Engineering* 124 (6): 653–63. doi:10.1061/(ASCE)0733-9445(1998)124:6(653).

Page, A. W. 1978. “Finite Element Model for Masonry.” *Journal of the Structural Division* 104 (8). ASCE: 1267–85. 1979. “A Model for the In-Plane Behaviour of Masonry and a Sensitivity Analysis of Its Critical Parameters.” In *5th International Brick Masonry Conference*, 262–67.

Page, Adrian W. 1979. “A Model for the In-Plane Behaviour of Masonry and a Sensitivity Analysis of Its Critical Parameters.” In *5th International Brick Masonry Conference*, 262–67.

Papa, E. 1996. “A Unilateral Damage Model for Masonry Based on a Homogenisation Procedure.” *Mechanics of Cohesive-Frictional Materials* 1 (February): 349–66.

Papastamatiou, D., and I. Psycharis. 1993. “Seismic Response of Classical Monuments—a Numerical Perspective Developed at the Temple of Apollo in Bassae, Greece.” *Terra Nova* 5 (6): 591–601. doi:10.1111/j.1365-3121.1993.tb00309.x.

Parisi, F., and N. Augenti. 2013. “Seismic Capacity of Irregular Unreinforced Masonry Walls with Openings.” *Earthquake Engineering & Structural Dynamics* 42 (1): 101–21.

Parisi, F., N. Augenti, and A. Prota. 2014. “Implications of the Spandrel Type on the Lateral Behavior of Unreinforced Masonry Walls.” *Earthquake Engineering & Structural Dynamics* 43 (12): 1867–87. doi:10.1002/eqe.2441.

Pelà, L., M. Cervera, and Pere Roca. 2011. “Continuum Damage Model for Orthotropic Materials: Application to Masonry.” *Computer Methods in Applied Mechanics and Engineering* 200 (9–12): 917–30. doi:10.1016/j.cma.2010.11.010.

Pelà, L., J. Bourgeois, P. Roca, M. Cervera, and M. Chiumenti. 2014a. “Analysis of the Effect of Provisional Ties on the Construction and Current Deformation of Mallorca Cathedral.” *International Journal of Architectural Heritage* in press (doi: 10.1080/15583058.2014.996920). Taylor & Francis. doi:10.1080/15583058.2014.996920.

Pelà, L., M. Cervera, S. Oller, and M. Chiumenti. 2014b. “A Localized Mapped Damage Model for Orthotropic Materials.” *Engineering Fracture Mechanics* 124–125: 196–216. doi:10.1016/j.engfracmech.2014.04.027.

Petracca, M., L. Pelà, R. Rossi, S. Oller, G. Camata, and E. Spacone. 2015. “Regularization of First Order Computational Homogenization for Multiscale Analysis of Masonry Structures.” *Computational Mechanics*, December. doi:10.1007/s00466-015-1230-6.

Petracca, M., L. Pelà, R. Rossi, S. Oller, G. Camata, and E. Spacone. 2017. “Multiscale Computational First Order Homogenization of Thick Shells for the Analysis of out-of-Plane Loaded Masonry Walls.” *Computer Methods in Applied Mechanics and Engineering* 315: 273–301. doi:10.1016/j.cma.2016.10.046.

Petromichelakis, Y., S. Saloustros and L. Pelà. 2014. “Seismic Assessment of Historical Masonry Construction Including Uncertainty.” In *Proceedings of EuroDyn 2014*, edited by Álvaro Cunha, Elsa Caetano, Pedro Ribeiro, Costas Papadimitriou, Carlos Moutinho, and Filipe Magalhães.

Rabczuk, T. 2012. “Computational Methods for Fracture in Brittle and Quasi-Brittle Solids : State-of-the-Art Review and Future Perspectives.” *ISRN Applied Mathematics* 2013: 1–61. doi:10.1155/2013/849231.

Roca, P., M. Cervera, G. Gariup, and L. Pelà. 2010. “Structural Analysis of Masonry Historical Constructions. Classical and Advanced Approaches.” *Archives of Computational Methods in Engineering* 17 (3): 299–325. doi:10.1007/s11831-010-9046-1.

Roca, P., M. Cervera, L. Pelà, R. Clemente, and Michele Chiumenti. 2013. “Continuum FE Models for the Analysis of Mallorca Cathedral.” *Engineering Structures* 46. Elsevier Ltd: 653–70. doi:10.1016/j.engstruct.2012.08.005.

Saloustros, S., L. Pelà, P. Roca, and J. Portal. 2014. “Numerical Analysis of Structural Damage in the Church of the Poblet Monastery.” *Engineering Failure Analysis* 48. Elsevier Ltd: 41–61. doi:10.1016/j.engfailanal.2014.10.015.

Saloustros, S., L. Pelà, and M. Cervera. 2015. “A Crack-Tracking Technique for Localized Cohesive-Frictional Damage.” *Engineering Fracture Mechanics* 150: 96–114. doi:10.1016/j.engfracmech.2015.10.039.

Saloustros, S., L. Pelà, M. Cervera, and P. Roca. 2016a. “A Macro-Modelling Finite Element Technique for the Realistic Simulation of Cracking in Masonry Structures.” *Structural Analysis of Historical Constructions - Anamnesis, Diagnosis, Therapy, Controls*, no. 2010: 284–90.

Saloustros, S., L. Pelà, M. Cervera, and P. Roca. 2016b. “Finite Element Modelling of Internal and Multiple Localized Cracks.” *Computational Mechanics*. Springer Berlin Heidelberg. doi:10.1007/s00466-016-1351-6.

Sarhosis, V., and Y. Sheng. 2014. "Identification of Material Parameters for Low Bond Strength Masonry." *Engineering Structures* 60. Elsevier Ltd: 100–110. doi:10.1016/j.engstruct.2013.12.013.

Slobbe, A.T., M.a.N. Hendriks, and J.G. Rots. 2014. "Smoothing the Propagation of Smeared Cracks." *Engineering Fracture Mechanics* 132 (December). Elsevier Ltd: 147–68. doi:10.1016/j.engfracmech.2014.10.020.

Theodossopoulos, D., and B. Sinha. 2013. "A Review of Analytical Methods in the Current Design Processes and Assessment of Performance of Masonry Structures." *Construction and Building Materials* 41: 990–1001. doi:10.1016/j.conbuildmat.2012.07.095.

Trovalusci, P., and R. Masiani. 2003. "Non-Linear Micropolar and Classical Continua for Anisotropic Discontinuous Materials." *International Journal of Solids and Structures* 40 (5): 1281–97. doi:10.1016/S0020-7683(02)00584-X.